

Measurements of scene spectral radiance variability

Juliette A. Seeley, Edward C. Wack, Daniel L. Mooney, Michael Muldoon, Shen Shey, Carolyn A. Upham, John M. Harvey, Richard N. Czerwinski, Michael P. Jordan, Alexandre Vallières*, Martin Chamberland*

MIT Lincoln Laboratory, 244 Wood Street, Lexington, MA, USA 02420-9185

*Telops, Inc. 100-2600 Avenue St-Jean-Baptiste Quebec City, Quebec, G2E 6J5 Canada

ABSTRACT

Detection performance of LWIR passive standoff chemical agent sensors is strongly influenced by various scene parameters, such as atmospheric conditions, temperature contrast, concentration-path length product (CL), agent absorption coefficient, and scene spectral variability. Although temperature contrast, CL, and agent absorption coefficient affect the detected signal in a predictable manner, fluctuations in background scene spectral radiance have less intuitive consequences. The spectral nature of the scene is not problematic in and of itself; instead it is spatial and temporal fluctuations in the scene spectral radiance that cannot be entirely corrected for with data processing. In addition, the consequence of such variability is a function of the spectral signature of the agent that is being detected and is thus different for each agent. To bracket the performance of background-limited (low sensor NEDN), passive standoff chemical sensors in the range of relevant conditions, assessment of real scene data is necessary¹. Currently, such data is not widely available². To begin to span the range of relevant scene conditions, we have acquired high fidelity scene spectral radiance measurements with a Telops FTIR imaging spectrometer³. We have acquired data in a variety of indoor and outdoor locations at different times of day and year. Some locations include indoor office environments, airports, urban and suburban scenes, waterways, and forest. We report agent-dependent clutter measurements for three of these backgrounds.

1. INTRODUCTION

To protect potential victims from a chemical attack, a variety of chemical detection systems have been and continue to be developed. Standoff systems, designed to sense the presence of chemical plumes at long range, are attractive because of the early warning advantage that they provide. They also provide coverage of a much larger area than point chemical sensors, which would need to be distributed much more abundantly to provide comparable coverage. The analytical technique that is most widely used for standoff sensing is long wave infrared (LWIR) spectroscopy, due to the availability of unique chemical signatures and the window in atmospheric absorption in this spectral region. LWIR spectroscopy may be conducted either actively (with the use of an IR source) or passively (using the blackbody radiation of the scene as the source). While passive standoff LWIR spectroscopy offers many advantages, such as greater on-the-move flexibility, and less complexity than a large and expensive laser system would introduce, using the scene spectral radiance as the source introduces its own complications that will be addressed in the following.

In a chemical sensing scenario, radiation received from the scene is a function of scene spectral radiance, plume absorption and emission, atmospheric absorption and emission, as well as absorption and emission, and potentially scattering of any other chemicals that are present in the environment.⁴ To estimate the radiance received at the sensor, the scene may be divided into many thin slices along the axis between the background and the sensor. If a hard background is present, it emits radiation according to its spectral emissivity and temperature. This radiation is absorbed by the slice of vapor adjacent to it, according to the temperature and specific vibrational modes of the chemical species. This slice may contain atmospheric gases, agent or other interfering chemicals. In addition to absorbing radiation, this slice also transmits some of the radiation emitted from the hard background and it emits radiation according to its own spectral emissivity and temperature. The net light that leaves this slice is then attenuated by the next slice, which also emits radiation. This is repeated through all of the slices between the background and the sensor. If the background is

This work was sponsored by the Department of the Air Force under Contract FA8721-05-C-0002. Opinions, interpretations, conclusions and recommendations are those of the authors and not necessarily endorsed by the United States Government.

warmer than the plume, the result is the background emission attenuated by the spectral signature of the chemical vapors present. The degree of attenuation depends on the concentration and path length of the plume and temperature difference between the plume and the background. This attenuation due to the chemical vapors is generally small compared to the total signal received by the sensor. Since this attenuation is the quantity that provides information about the plume, the relevant metric is not the signal itself but the differential signal --the difference between the radiance of the scene containing the plume and the scene without the plume. Making the assumption that the plume is thin and that the background radiance is known exactly, the expression for differential radiance becomes

$$(1) \Delta L \propto \Delta T \left. \frac{\partial B(T)}{\partial T} \right|_{T=T_s} cL\alpha_a$$

where ΔL is the differential radiance, ΔT is the temperature difference between the plume and the hard background, B is the Planck function at temperature T , c is the concentration of the plume, L is its path length, α is the absorption coefficient of the agent, and t_a is the atmospheric transmittance. This expression provides a simple way to determine the product of concentration and path length of a given agent if the temperature difference is known. However, it relies on the ability to completely subtract out the background, which may be difficult in a realistic sensing scenario.

There are various ways of estimating the plume-free spectrum to use for background subtraction. Since there is no *a priori* knowledge of the plume presence, no method is fail-proof. With a single-pixel spectrometer, the background may be obtained by assuming that the spectrum at a given time contains no plume and subtracting it from subsequent scans. This method assumes that the scene is constant in time; it is a good estimate if the scenery is not changing. More sophisticated algorithms attempt to address the problem of changing scenery using neural network algorithms⁵ to learn the background and classify detected signatures accordingly. When multiple-pixel information is available, as for a hyperspectral imager, the background of each pixel may be estimated, based on the spectral information of the other pixels⁶. This can be performed at varying degrees of complexity. The simplest approach is to approximate the background signature of each pixel as the mean spectrum of the entire scene. This approximation will be good when the plume is small compared to field of view (FOV) of the sensor, and the spectral information of the scene is spatially homogeneous. When various spectrally diverse components exist in the scene, the mean will not be a good estimate of the background. There are also methods to classify different components of a scene for better background estimation, but they always risk misclassifying the anomalous agent-containing pixels. Error in estimating the background translates directly into error in determining the chemical signature, thus spatial or temporal fluctuations of the scene spectral radiance can be problematic for agent detection.

The National Research Council (NRC) conducted a study¹ in 2003 to determine appropriate test protocols for standoff chemical sensing. One of their conclusions was that the current protocol neglected to account for the variable backgrounds that would be encountered in a real setting. One of their recommendations was to collect a variety of background spectra in a wide range of conditions and to combine these measured backgrounds with laboratory measurements of CWAs, concomitants and interferents. This would provide a representative set of spectra with which to perform testing. In the spirit of these recommendations, we have acquired data at various indoor and outdoor sites using a high fidelity LWIR hyperspectral imager from Telops Inc.³ We report a method of characterizing the scene spectral variability in the channels relevant for detection of particular CWAs for the various scenes we have investigated.

2. EXPERIMENTAL

The measurements were acquired with the Telops Inc. Field-portable Imaging Radiometric Spectrometer Technology (FIRST). This instrument is a lightweight and compact imaging radiometric spectrometer. The spectra measurements are performed using a Fourier-Transform Spectrometer (FTS). It uses a 320x256 LWIR PV-MCT focal plane array detector that can be windowed and formatted to fit the desired size and to decrease the acquisition time. The windows used for the results presented here are 256x256 and 256x196. Spectral resolution is user selectable and ranges from 0.25 to 150 cm^{-1} , with optimal system designed for 4 cm^{-1} . The resolutions that were used for the results reported here are 2, 4, and 8 cm^{-1} . This instrument gives the complete spectrum of each pixel in the image, each pixel having an instantaneous field-of-view of 0.35 mrad.

The instrument has 2 internal calibration blackbodies used to perform a complete end-to-end radiometric calibration of the measurements. In this study, they are also used to determine the contribution of the instrument to the total measured noise, so as to isolate scene-dependent effects. The LWIR version of the sensor used for this study has good sensitivity over the 8-12 μm band. This spectral band is ideal for standoff chemical agent detection at ambient temperatures. The sensor also has acquisition and processing electronics, including 4 GB of high-speed DDR-SDRAM, with the capability to convert the raw interferograms into spectra using real time Discrete-Fourier Transform (DFT).

The instrument outputs the measurements on a high-speed CameraLink interface. The configuration, monitoring and real-time housekeeping data collection is performed using an Ethernet link. A bore-sight video camera takes simultaneous visible images aligned with the imaging FTS. The instrument supports two operating modes: FTS mode and Camera mode. In Camera mode, the instrument generates standard broadband thermal IR digital video and supports up to 300 fps with the full 320x256 pixels of the focal plane array area. In FTS mode, the interferograms or the spectra are transferred along with a header containing all configuration parameters and monitored values to be stored on the computer.

LWIR background data was acquired with this sensor at various sites. The results presented here focus on the scenes described in Table 1.

Location	Scene components	Spectral resolution
Quebec City	River, sky, hills	2 cm^{-1}
Office hallway	Walls, floor and ceiling	4 cm^{-1}
Dahlgren, VA	Buildings, scaffolding, hills, sky, grass	8 cm^{-1}

Table 1: Background scenes

3. APPROACH

The detection performance of the sensor in a particular setting will not only depend on the properties of the agent plume, the internal noise of the sensor and the spectral fluctuations of the scene, but it will also depend on the spectral properties of the agent of interest in relation to the spectral fluctuations of the scene. If the scene spectral fluctuations are most prominent in spectral regions where the agent exhibits most of its absorption, they will more severely distort detection capability. Conversely, if most of the uncorrectable fluctuations occur in a spectral region where the matched filter is not interrogating for the presence of agent, they will not be as problematic. We have developed a procedure to assess the scene limited performance of individual scenes for particular agents.

The metric that we define in the following aims to characterize the performance-limiting scene noise. It is intended to be independent of sensor noise and plume properties, such as concentration and path length, but not agent identity, as explained previously. In attempt to isolate the scene noise from sensor noise, we have first discarded bad pixels. Telops Inc. has characterized the FIRST LWIR focal plane and provided a bad pixel map. This provided our first round of bad pixels. Second, since our goal was to isolate the pure scenes as much as possible, and ensure that the sensor noise floor was lower than the scene noise, we used very stringent requirements for declaring a pixel “good,” based on its spectral response. After identifying and removing spectrally deviant pixels, we calculated the agent-dependent spectral noise of the sensor, using the sensor’s internal blackbody calibration sources. We calculated the agent-dependent spectral noise of the measured scene, which inevitably includes contribution from the sensor, and we combined the two in a metric that we refer to as the effective noise, σ_{eff} . The effective noise metric attempts to quantify the spectral noise induced by the scene itself, with respect to a specific chemical agent.

The bad pixels were determined on a spectral basis. To measure the calibrated spectral response of each pixel without the presence of a background, ten data frames were acquired with each blackbody source filling the sensor field of view, for a total of 20 blackbody frames. There was a temperature difference of 10K between the two sources. The resulting data was used to calculate the complex gain and offset for each pixel, to be used for radiometric calibration. The gains

and offsets were then subsequently used to calibrate each of the same 20 blackbody frames. The spectrum of each pixel, s_i , viewing only the hot source, was represented by a point in n -dimensional space, where n is the number of spectral channels. The Mahalanobis distance, d_i , the distance between the i^{th} pixel and the mean spectrum of all of the pixels, was determined for each pixel and outlier pixels were removed from the good pixel map. The Mahalanobis distance for each of P pixels, defined in Equation 2, was computed using the covariance matrix, Σ , and mean, μ , of only the pixels included in Telops' good pixel map. This minimized their contamination by bad pixels. This process was repeated for all 20 frames, until any pixel that did not fall very close to the mean spectrum was discarded. It should be noted that many of the pixels that were discarded are not necessarily bad pixels and might be acceptable for use in a real sensing scenario. However, for this application the goal was to remove as much of the sensor contribution as possible, so we erred on the side of throwing away too many pixels.

$$d_i = \langle (s_i - \mu) | \Sigma^{-1} | (s_i - \mu) \rangle,$$

$$(2) \quad \Sigma = \frac{\sum_{i=1}^P |s_i - \mu\rangle \langle s_i - \mu|}{P}$$

To characterize the sensor noise in the spectral channels of interest for a particular agent with absorption coefficient, α , we define the metric, σ_{CAL} . This is the magnitude of the agent signal divided by the square root of the matched-filter enhanced signal-to-noise ratio squared, SNR^2_{MF} , of the sensor when observing a calibration source. Equation 3 illustrates that the agent concentration, path length, and temperature differential cancel out of this expression; this metric is dependent upon agent identity but not on other properties of the threat.

$$(3) \quad \sigma_{CAL} = \frac{\sqrt{\langle \alpha | \alpha \rangle}}{\sqrt{SNR^2_{MF,CAL}}},$$

$$SNR^2_{MF,CAL} = \langle \alpha | \Sigma_{CAL}^{-1} | \alpha \rangle$$

This metric has units of spectral radiance noise; it is the magnitude of the signal divided by the signal-to-noise. This is only representative of sensor performance if a similar matched filter is actually used for detection. The matched filter that provides this signal-to-noise ratio maximizes the signal-to-noise by de-weighting noisy channels. Additionally, by transforming the signal into a basis in which the scene noise is diagonal, we deal with the noise correlation between spectral channels in an optimal way that may help to reduce its effect. This metric provides the noise information in the channels relevant for only the agent of interest because eigenvectors of the agent with no absorption features, when transformed into the space of the covariance matrix, will have no overlap with the covariance matrix. Thus only the regions of the spectrum with agent spectral features will be considered. A similar metric was used to characterize the measured scene data of various backgrounds with the scene covariance matrix of each background.

$$(4) \quad \sigma_{tot} = \frac{\sqrt{\langle \alpha | \alpha \rangle}}{\sqrt{SNR^2_{MF,tot}}},$$

$$SNR^2_{MF,tot} = \langle \alpha | \Sigma_{tot}^{-1} | \alpha \rangle$$

To characterize the spectral fluctuations of the scene itself relative to the fluctuations of the sensor, we define the effective noise, σ_{eff} in equation 5. The effective scene noise is the measured noise corrected for the sensor noise, both defined above. This definition assumes that the noise measured while observing the calibration source is dominated by the sensor itself, and not the calibration source. This is a good assumption since the temperature of the source should not be rapidly fluctuating, nor should temperature fluctuations result in differences in narrow spectral features.

$$(5) \quad \sigma_{eff} = \sqrt{\sigma_{tot}^2 - \sigma_{CAL}^2}$$

Although we have chosen to observe the spectral fluctuations as a function of spatial position in this work, they can also be assessed as a function of time. While the spatial fluctuations are the relevant metric when using a hyperspectral imager, the temporal fluctuations are the important quantity when using a single pixel instrument. The relevant domain depends upon how the background is estimated.

4. RESULTS

We have investigated three different scenes, described in table 1, an indoor hallway, a natural scene including river, hills and sky, and a scene of more urban appearance, including many different materials and buildings. In all three cases, we only considered the spectral range 900-1250 cm^{-1} . This ensured that the large spectral fluctuations that occur at the edges of the spectral range of the focal plane were avoided. We used a total of 20 blackbody scenes to obtain the estimate of the effective sensor noise, and 20 scene frames to obtain the estimate of the effective total noise. More frames should be used to obtain higher confidence in the results. However, qualitative relationships may be deduced from these results, and general trends observed. We have found that the indoor hallway and urban-like scene did not have substantial effective noise, whereas the natural scene did have considerable effective noise with respect to sarin and mustard HD vapor.

Indoor Hallway

We created a broadband LWIR image of each scene by averaging the radiance signal over all spectral bands. Because the sensitivity of the sensor falls off at the edges of the spectral range, to minimize noise in these images, again we used only the radiance in the spectral range, 900-1250 cm^{-1} . It is still possible to obtain spectral information outside of this range, but in terms of imaging, using radiance beyond this range was not beneficial for most scenes that we visualized. Bad pixels, identified by Telops, were corrected by assigning each bad pixel the median value of its nearest neighbors. The image shown on the left side of figure 2 was acquired in an indoor hallway of an office environment. Clearly, there was very little temperature contrast or variation of spectral emissivity in this scene. The covariance matrix used to calculate the effective noise for this scene is shown on the right. This covariance matrix exhibits very little off-diagonal covariance. This indicates that there is very little correlated noise in the scene between spectral channels. The broadband image concurs that there is very little temperature change across the scene. The variation of intensity along the diagonal of the covariance matrix indicates that there is more noise at the edges of the spectral range, where the sensitivity of the focal plane falls off.

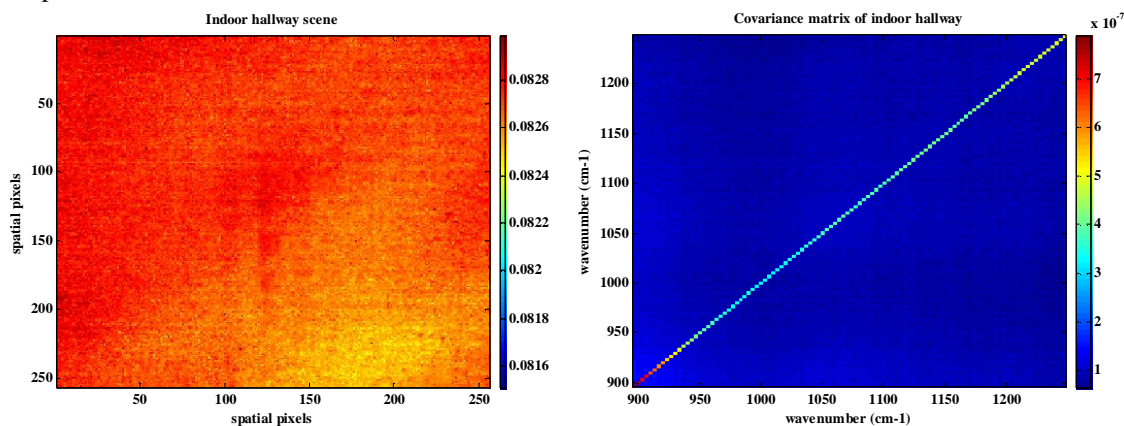


Figure 1: Indoor hallway broadband image (in units of radiance, $\text{W/m}^2 \text{sr cm}^{-1}$) (left) and covariance matrix (in units of spectral radiance squared, $(\text{W/m sr cm}^{-1})^2$) (right)

The effective noise values of this scene relative to sarin and mustard HD vapor were computed and tabulated in table 2. We find that the indoor hallway scene does not appear to contain much more spectral fluctuation than the calibration sources that we compare it to. The fact that the spectral fluctuations are greater with respect to mustard, whose primary

absorption feature occurs near the edge of the spectral range, is possibly a result of the more highly fluctuating response of the focal plane at that spectral band, which makes measurements in that region inherently less reliable.

Agent	σ_{CAL}	σ_{tot}	σ_{eff}
Sarin	5.1×10^{-4}	5.6×10^{-4}	2.3×10^{-4}
Mustard HD	6.7×10^{-4}	7.5×10^{-4}	3.4×10^{-4}

Table 2: Effective noise values for indoor hallway scene (units of Watts/m² sr cm⁻¹)

Dahlgren, VA

The second scene we present was acquired near the Potomac River in Dahlgren, Virginia with 8 cm⁻¹ resolution and 256x256 spatial pixels. This scene exhibits much more diversity than the indoor hallway scene, as seen in the broadband image shown on the left in figure 3. It was processed in a manner similar to the image shown in figure 3. Again, the covariance matrix of this scene is shown on the right side of figure 2. It is clear that the scene is highly correlated at the small wavenumbers and less correlated at larger wavenumbers. By inspection, one might assume that the variation in scene spectral radiance for this scene would be problematic because of a much greater temperature contrast relative to the indoor scene. However, the matched filter enhanced signal-to-noise exploits correlation in the background scene to correct for variations that happen in a predictable manner. The matched filter enhanced signal-to-noise ratio accounts for the SNR enhancement that taking advantage of correlation provides.

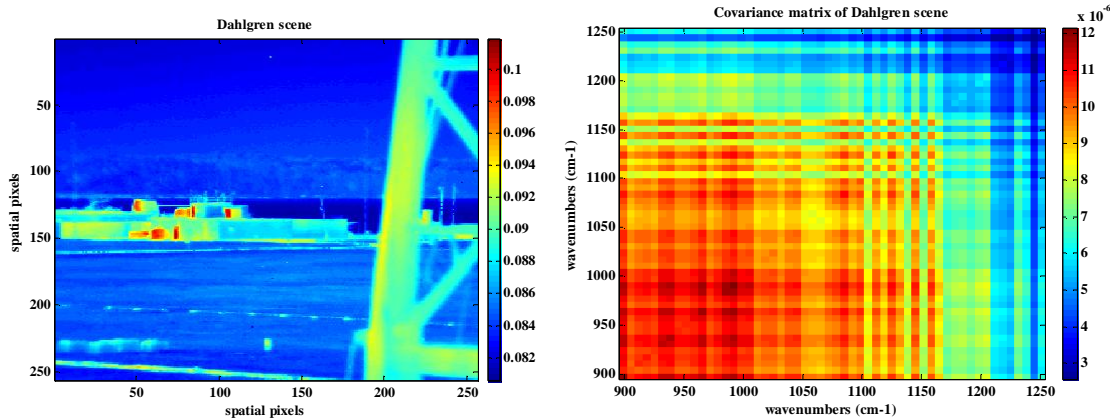


Figure 2: Dahlgren, VA broadband image (in units of radiance, W/m² sr cm⁻¹) (left) and covariance matrix (in units of spectral radiance squared, (W/m sr cm⁻¹)²) (right)

The effective noise values listed in table 3 indicate that exploiting the correlated nature of the scene radiance is effective in removing a great deal of the background fluctuation. The values listed in the table reflect the remaining uncorrelated noise that cannot be corrected for. Until a systematic study is performed to determine exactly what is causing the difference in effective calibration noise between data sets and how it is affected by blackbody temperature and spectral resolution, a quantitative comparison is premature. But, generally, we do find that the effective noise of this scene is significantly higher than the calibration effective noise, similar to the indoor hallway scene, which we know has very little spectral variation. This result indicates that the spectral variability of a scene may not be predicted by merely observing broadband image. Scenes that appear to have large variations may contain enough correlation between spectral channels that much of the variability may be removed.

Agent	σ_{CAL}	σ_{tot}	σ_{eff}
Sarin	4.2×10^{-4}	5.3×10^{-4}	3.2×10^{-4}
Mustard HD	5.2×10^{-4}	6.2×10^{-4}	3.4×10^{-4}

Table 3: Effective noise values for Dahlgren, VA scene (units of Watts/m² sr cm⁻¹)

Quebec City

The final scene that we present was acquired in Quebec City, looking at the river, hills and sky. It was acquired with 2 cm^{-1} spectral resolution with a spatial window of 256×196 pixels. Again, the broadband image of the scene is shown on the left of figure 3 and its covariance matrix is shown on the right. Similar to the scene in Dahlgren, VA, there is substantial intensity in the off-diagonal elements of the matrix, indicating a high degree of spectral correlation among pixels.

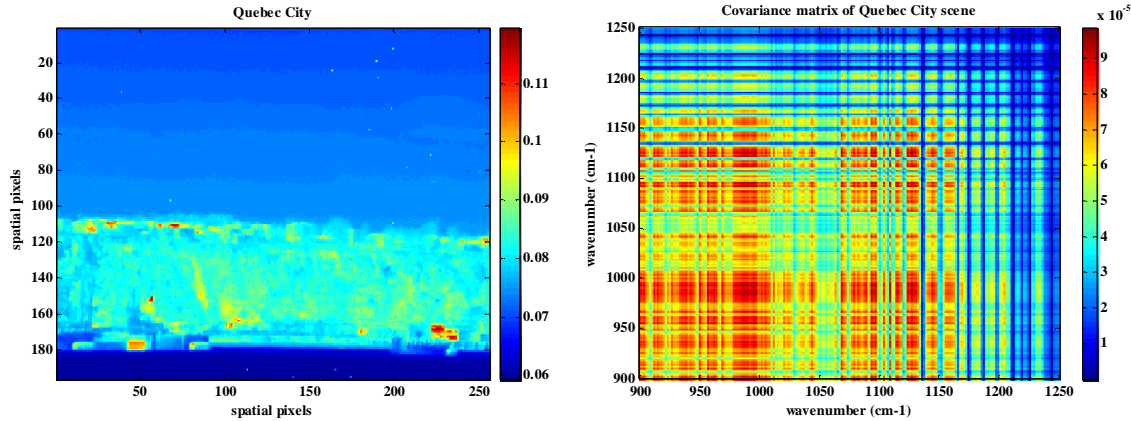


Figure 3: Quebec City broadband image (in units of radiance, $\text{W/m}^2 \text{ sr cm}^{-1}$) (left) and covariance matrix (in units of spectral radiance squared, $(\text{W/m sr cm}^{-1})^2$) (right)

Although this scene exhibits substantial noise correlation among spectral channels, there is still substantial residual noise after the matched filter operation has been performed. Again, a direct comparison between scenes is probably not warranted at this time, but it is clear that the effective noise of the scene is large compared to the calibration effective noise.

Agent	σ_{CAL}	σ_{tot}	σ_{eff}
Sarin	7.3×10^{-4}	10.7×10^{-4}	7.8×10^{-4}
Mustard HD	8.5×10^{-4}	11.1×10^{-4}	7.1×10^{-4}

Table 4: Effective noise values for Quebec City scene (units of $\text{Watts/m}^2 \text{ sr cm}^{-1}$)

By inspection, it seemed that this residual noise was a result of mixing spectrally diverse components: sky, hill and water. To further investigate, we calculated the effective noise for homogeneous portions of the scene, expecting to find that each component had much lower effective noise than the scene as a whole. Although this was the case for the sky and hill, it was not true for the river. The values are tabulated in table 5. The noise value for the river portion of the scene was somewhat higher than the other scene components. The sky and hill are relatively spectrally constant. We expect the water to be spectrally homogeneous since liquid water has a relatively flat spectral response. However, it exhibits the most effective scene noise.

Scene component(Agent)	σ_{CAL}	σ_{tot}	σ_{eff}
Sky (Sarin)	5.8×10^{-4}	7.5×10^{-4}	4.8×10^{-4}
Sky (Mustard HD)	6.7×10^{-4}	8.0×10^{-4}	4.4×10^{-4}
Hill (Sarin)	6.1×10^{-4}	7.8×10^{-4}	4.7×10^{-4}
Hill (Mustard HD)	7.1×10^{-4}	8.9×10^{-4}	5.7×10^{-4}
River (Sarin)	6.5×10^{-4}	$10. \times 10^{-4}$	1×10^{-3}
River (Mustard HD)	7.6×10^{-4}	11×10^{-4}	1.1×10^{-3}

Table 5: Effective noise values for different components of Quebec City scene (units of $\text{Watts/m}^2 \text{ sr cm}^{-1}$)

To begin to understand this effect, we have further investigated these three portions of the scene. First, we plot a spectrum of each of three pixels taken from the portions of the scene named in table 5.

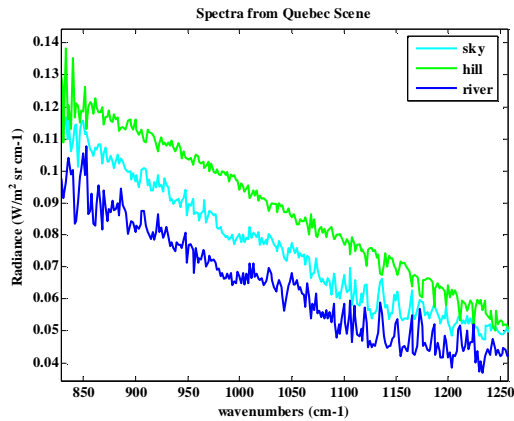


Figure 4: Scene spectra of components of Quebec City view

According to the low radiance value of the pixel looking at the river, it radiates the least energy. Inspection of the broadband image confirms that this portion of the scene is coldest. The structure of the spectrum indicates that water vapor between the sensor and the river is emitting. The lines between 1100 and 1250 cm^{-1} , shown in figure 4, match with the lines in the library water vapor spectrum⁷. The pixel observing the sky has a higher temperature, as indicated by its higher intensity in figure 4 and brighter overall radiance in figure 3. Water vapor in the path between the sky and the sensor is also emitting. Its emission features are somewhat smaller than the emission features of the vapor over the river. Although the sky path length is much longer, the temperature contrast between the river and water vapor is greater, and perhaps the concentration of water is greater directly above the river. Both of these effects could explain why the emission of the water vapor is greater over the cold river than through the atmosphere. On the other hand, the pixel observing the hill shows negative peaks in its intensity, indicative of water vapor absorption. The hill is not only warmer than the water or sky, as seen by its intensity, but the fact that the water vapor absorbs in this region signifies that the hill is also warmer than the air.

Quebec City: River pixels

Upon observation of the covariance matrix of only river pixels, we notice that the correlation between spectral channels occurs at much narrower wavenumber bands than it does over the entire scene. The spectral channels whose noise is largely correlated to other channels coincide with the water vapor absorption lines. These correlated channels also have higher noise along the diagonal. On the right hand side of figure 5 the square root of the diagonal of the covariance matrix is overlaid on a library spectrum of water vapor, to illustrate that the noise occurs at the water vapor lines.

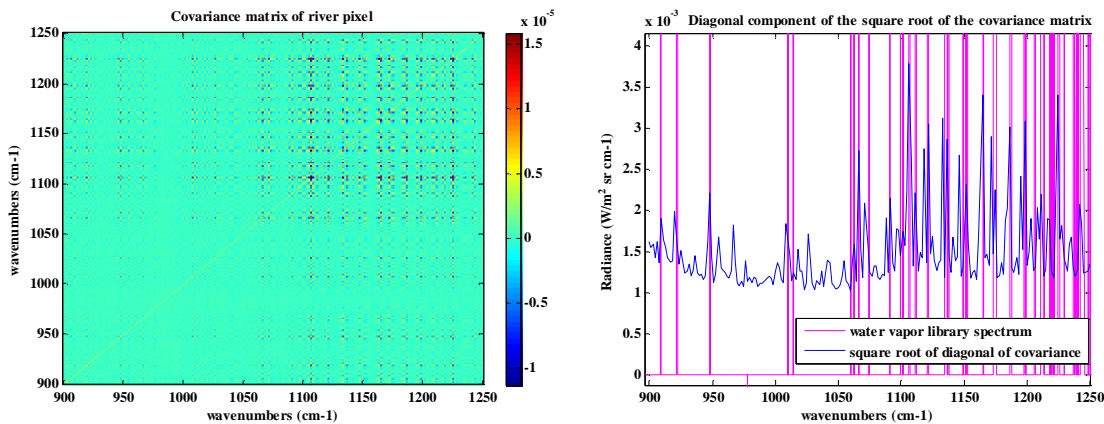


Figure 5: Covariance of river pixels matrix (left, in units of spectral radiance squared, $(\text{W/m sr cm}^{-1})^2$), square root of diagonal of the covariance matrix (right)

One interpretation of this result is that the water vapor concentration or path length is changing from pixel to pixel and that this contributes to spectral fluctuations in this portion of the scene. One possible explanation for the higher effective noise in the river pixels is the changing emissivity of the water as the viewing angle of light varies while looking at different facets of the water surface. Validation of this hypothesis requires further investigation.

Quebec City: Sky pixels

For comparison, we have also observed a similar slice of the sky pixels (only 10 pixels high and 256 across). The covariance matrix is shown on the left in figure 6. Similar to the river pixels, many of the bands exhibiting high correlation coincide with water vapor absorption lines. Negative covariances occur between channels where one is emitting and the other is not. As shown on the right side of figure 6, the river pixels exhibit more correlation in the larger wavenumber channels while the sky pixels are more correlated in the smaller wavenumber channels. This needs to be studied further.

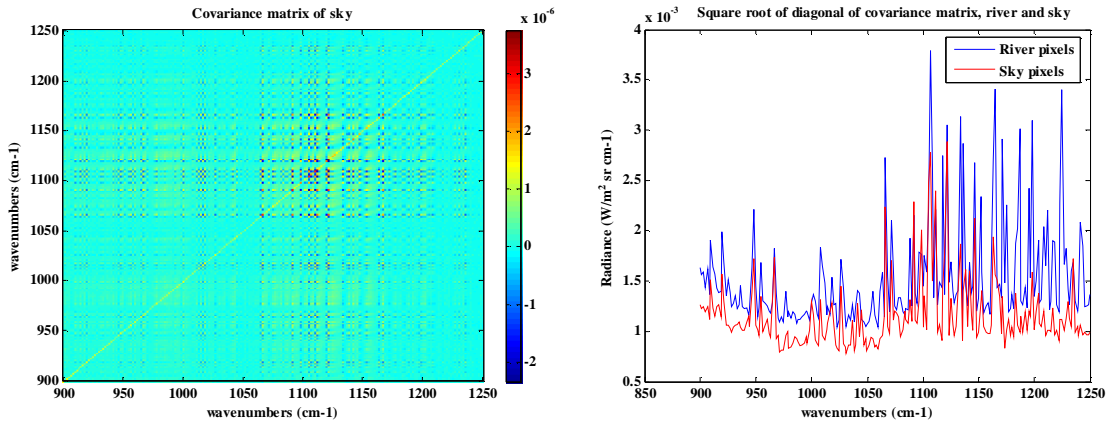


Figure 6: Covariance of small slice of sky pixels (sky 1) (left, in units of $(W/m\ sr\ cm^{-1})^2$), square root of diagonal of the covariance matrix (right)

Next we have observed progressively taller slices of sky to observe how the covariance matrix responds. We begin with a very short slice of highest altitude sky, which extends across the whole x-axis of the image and down to the 10th pixel in the y dimension, designated sky 1. The results were shown in figure 6. The second slice extends from the top of the image down to the 30th pixel. Sky 3 refers to pixels from pixel 1 down to pixel 50. Sky 4 extends to pixel 60 and sky 5 to pixel 90. Figure 7 illustrates the portion of the image included in each sky slice.

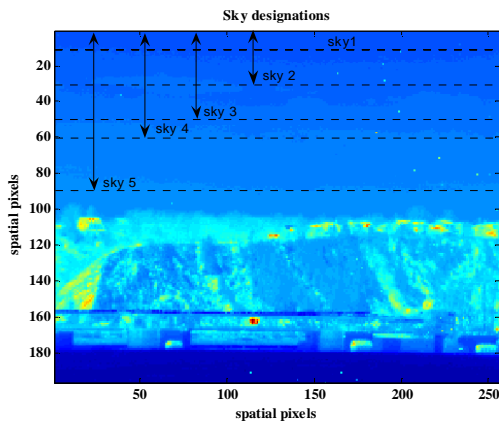


Figure 7: Sky slice designations

When increasing from only 10 pixels tall to 30 pixels tall (sky 2, left) the sharpness of the correlations is smoothed as the spaces between them become more correlated, most likely due to the larger range of sky temperature that is captured in this taller slice. Additionally, correlation at the ozone absorption bands is observed, indicating that we are now viewing pixels with different concentrations of ozone, as is expected with this wider range of altitudes. This effect is accentuated as taller slices of sky are observed. The right side of figure 8 is the covariance matrix of a 50 pixel tall slice (sky 3).

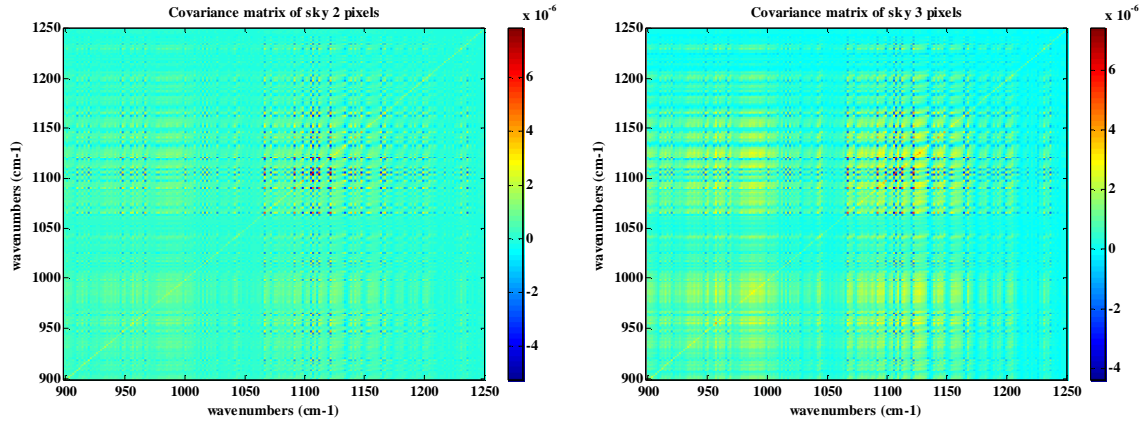


Figure 8: Covariance of different slices of sky pixels (sky 2& 3) (in units of $(W/m\ sr\ cm^{-1})^2$)

This is repeated for a 60 pixel tall slice (top) and finally a 90 pixel tall slice (bottom). When we increase the height of the window beyond 50 pixels, we see that the channels that are more correlated occur where there are no water lines or ozone lines. When the height of the slice becomes tall enough, correlation due to temperature difference dominates correlation due to the water lines; the spectral regions where there are no lines become more correlated. The ozone absorption bands are evident in the plot of the square root of the covariance matrix diagonal (right). This trend of temperature domination of correlation increases as a wider range of altitudes becomes present, as seen between top and bottom of figure 9.

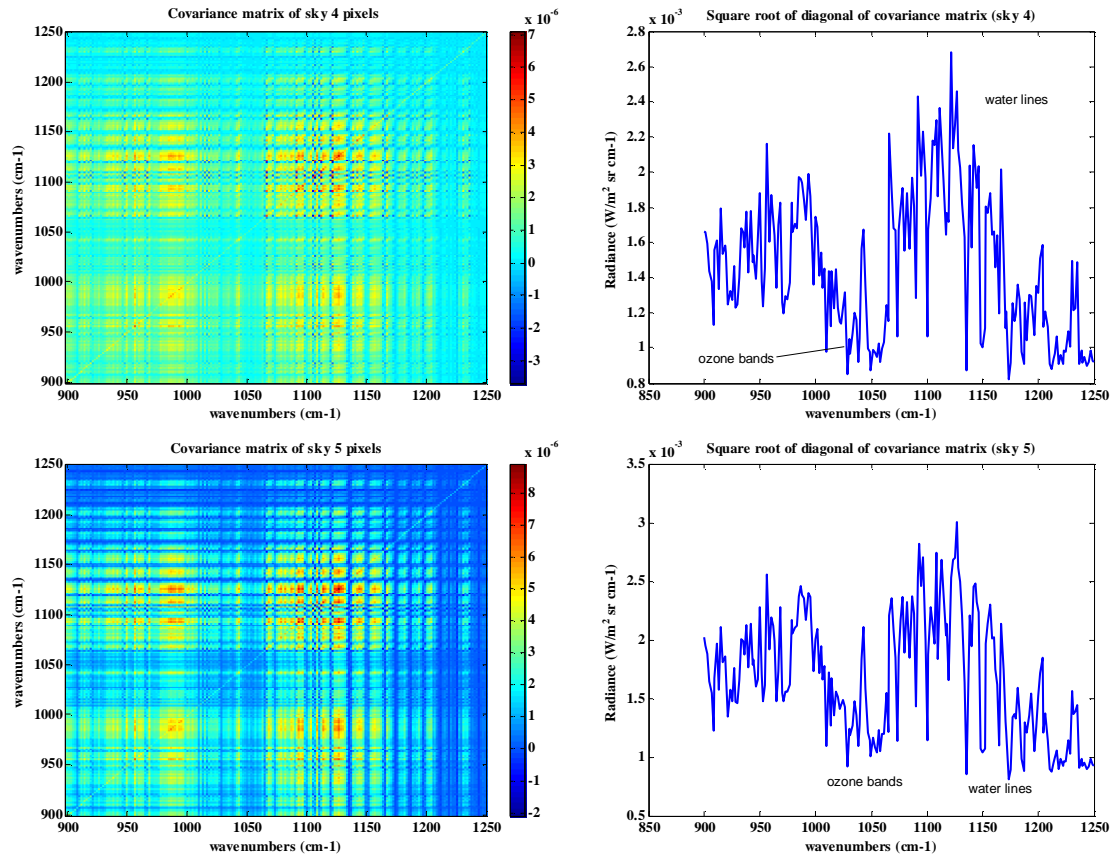


Figure 9: Covariance of different slices of sky pixels (sky 4&5) (left, in units of $(W/m\ sr\ cm^{-1})^2$), square root of diagonal of covariance matrix (right)

5. CONCLUSIONS

We have investigated LWIR hyperspectral data cubes acquired with a Telops FIRST sensor³ in three different backgrounds: an indoor hallway, a scene of urban appearance in Dahlgren, VA and a more natural scene in Quebec City. We have developed metrics to assess the degree of fluctuation in scene spectral radiance relative to the spectral features of sarin and sulfur mustard. The metric, effective noise, is intended to isolate the scene radiance noise from the sensor radiance noise. It reflects the scene spectral radiance fluctuation remaining after spectral correlation from pixel to pixel has been exploited, as would occur with the use of a matched filter detector.

We have found that the effective noise measured for each scene while observing the calibration sources only was not the same from data set to data set. It is still to be determined how this particular metric is affected by the temperature of the calibration source and the spectral resolution. However, some general trends have been observed. The indoor scene, with very little temperature contrast, exhibits very little correlated noise and has a small effective noise value. Although the scene of urban appearance obviously has high temperature contrast and high correlated noise, the effective noise is not large since variation in the scene spectral radiance due to the different temperatures is dealt with in an optimal way by using a matched filter. The scene of natural appearance, also exhibiting large correlated noise, has a significant effective noise value. Our results imply that the amount of scene spectral radiance may not be predicted by observing a broadband image only. A scene with high temperature contrast will not necessarily be a difficult environment in which to detect a chemical agent. Although the spectral radiance does vary from pixel to pixel, the use of a matched filter detector deals with that correlation in an optimum way. Upon further refinement of our metric, it will be used to assess the ability to detect specific chemical agents in specific environments.

6. REFERENCES

- 1.) "Test and Evaluation of Standoff Chemical Agent Detectors", by Committee on Testing and Evaluation of Standoff Chemical Agent Detectors and Board on Chemical Sciences and Technology, National Research Council, The National Academies Press, 2003.
- 2.) D. F. Flanigan, A.C. Samuels, C. Zhu, F. D'Amico, "Noise, Clutter and Determinism in IR Spectral Signatures Under Varying Meteorological Conditions", Fifth Joint Conference on Standoff Detection CW BW Defense, Williamsburg, VA, 2004.
- 3.) V. Farley, C. Belzile, M. Chamberland, *et al.* "Development and testing of a hyper-spectral imaging instrument for field spectroscopy", SPIE Proceedings **5546-02**, 2004.
- 4.) R. Harig, "Passive remote sensing of pollutant clouds by Fourier-transform infrared spectrometry: signal-to-noise ratio as a function of spectral resolution," *Applied Optics* **43:23**, 2004.
- 5.) S. Subramanian, N. Gat, M. Sheffield, J. Barhen, N. Toomarian, "Methodology for hyperspectral image classification using novel neural network", in *Multispectral and Hyperspectral Imagery III*, SPIE, **3071**, 1997.
- 6.) S. Orloff, B. Weinberg, G.A. Shaw, S-M. Hsu, C.A. Upham, J.B. Evans, K.G. Heinemann, "Investigation of Supervised Background Classification Algorithms on Hyperspectral Data," Lincoln Laboratory Project Report HTAP-4, 2002.
- 7.) S.W. Sharpe, *et al.*, "A quantitative infrared spectral library of vapor phase chemicals: applications to environmental monitoring and homeland defense," in *Chemical and Biological Standoff Detection II*, J.O. Jensen and J.-M. Theriault, eds., Proc. SPIE **5584**, 2004.